



## Full length article

## Phase-field simulation of coherent BCC/B2 microstructures in high entropy alloys

J.L. Li<sup>a</sup>, Z. Li<sup>b,\*</sup>, Q. Wang<sup>a,\*</sup>, C. Dong<sup>a</sup>, P.K. Liaw<sup>c</sup><sup>a</sup> Key Laboratory of Materials Modification by Laser, Ion and Electron Beams (Ministry of Education), School of Materials Science and Engineering, Dalian University of Technology, Dalian 116024, Liaoning, China<sup>b</sup> School of Mechanical Engineering, Dalian University of Technology, Dalian 116024, Liaoning, China<sup>c</sup> Department of Materials Science and Engineering, The University of Tennessee, Knoxville, 37996, Tennessee, USA

## ARTICLE INFO

## Article history:

Received 14 February 2020

Revised 4 July 2020

Accepted 9 July 2020

Available online 15 July 2020

## Keywords:

Phase-field simulation

High-entropy alloys

Coherent microstructure

Precipitate morphology

Microstructural evolution

## ABSTRACT

This present work simulated the coherent BCC/B2 microstructures existing in body-centered-cubic (BCC)-based Al-Ni-Co-Fe-Cr high entropy alloys (HEAs) in light of the phase-field method. These coherent BCC/B2 microstructures contain spherical or cuboidal nanoprecipitates, or exhibit a weave-like spinodal decomposition in experiments. Based on the Chan-Hilliard equation, a two-dimensional phase field model was established using the COMSOL Multiphysics software to reveal the coherent microstructural evolutions of the present HEAs. It was found that the simulations of spherical/cuboidal nanoprecipitations and weave-like spinodal decomposition are well consistent with the experimental results. Both the lattice misfit and the anisotropy difference of Young's moduli between the precipitated phase and matrix phase affect the precipitate morphology, in which the cuboidal nanoprecipitation is especially susceptible to the modulus anisotropy. The coarsening behavior of precipitates is also discussed with the aid of the simulation results. The phase-field simulation will provide an important technique to predict the microstructural evolution and to assist the composition design of new HEAs.

© 2020 Acta Materialia Inc. Published by Elsevier Ltd. All rights reserved.

## 1. Introduction

Unique coherent microstructures with ordered nanoprecipitates into the disordered solid solution matrix are always expected for engineering alloys to achieve prominent mechanical properties at high temperatures (HTs), which has incarnated well into Ni-base superalloys [1,2]. Especially, the coherent microstructure with cuboidal ordered L1<sub>2</sub> γ'-Ni<sub>3</sub>Al (*cP*-Cu<sub>3</sub>Au type) nanoprecipitates into the face-centered-cubic (FCC) γ matrix renders the Ni-base single superalloys with excellent HT creep-resistant properties above 1273 K [3,4]. Actually, the shape, size and volume fraction of ordered precipitates could affect the HT mechanical properties of alloys. The achievement of cuboidal γ' nanoprecipitates was attributed to a moderate lattice misfit ( $\varepsilon \sim \pm 0.4\%$ ) between γ and γ' phases, which was implemented through adding multiple elements to adjust the lattice constants of γ and γ' simultaneously [3,4]. However, for the coherent microstructures with ordered B2-NiAl (*cP*-CsCl type) phase strengthening the disordered body-centered-cubic (BCC) solid solution matrix, it is difficult to

realize such cuboidal coherent nanoprecipitation in BCC-based alloys. It mainly resulted from the unfavorable lattice misfit caused by the large composition difference between BCC and B2 phases, in which a weave-like spinodal decomposition was always formed [5,6]. Interestingly, in a Fe-based ferritic steel (Fe-12.7Al-9Ni-10.2Cr-1.9Mo at.%, abbreviated as FBB-8), spherical B2-NiAl nanoparticles were coherently precipitated into the BCC matrix due to a small lattice misfit of  $\varepsilon = 0.06\%$ , resulting in an outstanding creep resistance at 973 K, better than the conventional P92, P122, and 12CR steels strengthened by carbides [7–11]. Thereof, it would be expected to obtain a moderate lattice misfit in B2-strengthened BCC alloys through co-adjusting the compositions of BCC and B2 phases in multi-component systems.

Recently, a new kind of compositionally complex alloys have been developed, which is always addressed as high-entropy alloys (HEAs) since they contain multiple principal elements with equimolar, near-equimolar or non-equimolar mixing [12–14]. Nevertheless, simple crystalline structures, such as FCC, BCC, hexagonal-close-packed (HCP) phases and their ordered derivatives, would like to be formed [12–16]. HEAs have attracted much more interests due to their unique microstructures and diverse properties [17–20]. Typically, in BCC/B2 HEAs constituted of Al and transition metals (TMs), we obtained special coherent

\* Corresponding authors.

E-mail addresses: [lizhen@dlut.edu.cn](mailto:lizhen@dlut.edu.cn) (Z. Li), [wangq@dlut.edu.cn](mailto:wangq@dlut.edu.cn) (Q. Wang).

microstructures with spherical and cuboidal B2 nanoprecipitates in the BCC matrix through a cluster formula approach for the design of alloy compositions [21]. In particular, the cuboidal B2 nanoprecipitates could appear in BCC-based Al<sub>2</sub>TM<sub>14</sub> HEAs due to a moderate  $\varepsilon = 0.4 \sim 0.6\%$ , in which Al is fixed and TMs are the combinations of Ni, Co, Fe, and Cr. Such kind of HEAs exhibit high strength, good ductility, as well as high microstructural stability at elevated temperatures [22]. Increasing the Al amount, a weave-like spinodal decomposition microstructure would like to appear due to a relatively larger  $\varepsilon$ , which could result in an embrittlement [23]. In fact, it is still a challenge to control the coherent microstructures with different morphologies precisely in BCC/B2-based alloys till now.

For better understanding of coherent microstructures in various alloy systems, the phase-field method was generally used to simulate and to predict the microstructural evolution, especially the morphological evolution of the second-phase precipitates [24]. It is beneficial to understand the underlying mechanisms during the solidification and the solid-state phase transformations [25–32]. This method has been become a powerful computational approach to deal with many types of microstructural variations [33–38], in which a successful instance is that it has been widely applied into the Ni-base superalloys to simulate the morphological evolution of  $\gamma'$  precipitates, including the particle coarsening during heat treatments and the particle rafting under applied stress fields [39–45]. These simulations can provide an important support for profound understanding of experimental results. For the coherent microstructure of BCC/B2, more phase-field simulations focused on the microstructural evolution of weave-like spinodal decomposition since this kind of microstructure is the most common appeared experimentally in conventional BCC/B2-based alloys. Therefore, in the present work, the phase-field method will be introduced to simulate the evolutions of three typical coherent microstructures experimentally obtained in HEAs, including spherical and cuboidal nanoparticles, as well as weave-like BCC/B2 microstructure. Then, the influence of the elastic anisotropy difference between BCC and B2 on the nanoparticle morphologies will be primarily discussed, in which the elastic anisotropy deference is the key factor to determine the particle morphology when the lattice misfit is relatively large. The phase-field method will provide an important theoretical basis for predicting the microstructural evolution and assisting the composition design of new HEAs.

## 2. Phase-field method

### 2.1. Phase-field model

Phase transformation processes are generally driven by the minimization of the total free energy, which consists of chemical, interfacial, elastic, plastic, and magnetic contributions, etc. [46]. Several phase-field models have been built to illuminate this transition process, among which the classical Cahn–Hilliard nonlinear diffusion model was developed from a spinodal phase decomposition in binary alloy systems to describe the conserved concentration field [47,48]. Since the disordering-ordering transition of BCC and B2 phases is always attributed to the spinodal decomposition [49], the Cahn–Hilliard equation is introduced into the present work to describe the microstructural evolution in elastically inhomogeneous system. Then the total free energy of the system includes the chemical free energy  $F^{\text{ch}}$  and elastic energy  $F^{\text{el}}$ , in which the former  $F^{\text{ch}}$  is composed of the bulk free energy and the gradient interfacial energy [50]. Specifically, the chemical energy is related to the alloy composition, while the elastic energy is dependent on the elastic stress field during phase transformation, in which the elastic stress is induced by either a lattice misfit between the precipitated phase and the matrix or an artificial applied load [33,51].

For a binary phase decomposition alloy system with a miscibility gap, an alloy of the composition  $c'$  will consist of two equilibrium phases, the matrix phase and the precipitated phase with compositions  $c_m'$  and  $c_p'$ , respectively [52,53]. The composition variable  $c'$  could be rescaled to a scalar composition  $c$  with Eq. (1):

$$c = \frac{c' - c_m'}{c_p' - c_m'} \quad (1)$$

With this definition, the scaled composition  $c$  of a two-phase alloy will be the same as the equilibrium volume fraction of the precipitated phase.

In the present phase-field model for spinodal decomposition, an instantaneous configuration could be described in terms of the position ( $r$ )- and the time ( $t$ )-dependent concentration field variable  $c(r, t)$ . Thus, the classical Cahn–Hilliard model is expressed with Eq. (2):

$$\frac{\partial c(r, t)}{\partial t} = \nabla \left( M \nabla \frac{\delta F}{\delta c(r, t)} \right) = \nabla \left( M \nabla \frac{\delta (F^{\text{ch}} + F^{\text{el}})}{\delta c(r, t)} \right) \quad (2)$$

where  $c$  is the scaled composition,  $M$  is the kinetic coefficient that characterizes the chemical mobility related to the interdiffusivity, and  $F$  is total free energy. Among them, the chemical free energy  $F^{\text{ch}}$  could be given by Eq. (3):

$$F^{\text{ch}} = N_V \int_V [f(c) + \kappa (\nabla c)^2] dV \quad (3)$$

in which  $N_V$  is the number of atoms per unit volume,  $f(c)$  is the bulk free energy density, and  $\kappa$  is the gradient energy coefficient dependent on both the composition  $c$  and temperature. Generally,  $\kappa$  is a constant value for a regular solution [47].

In the present Al–Ni–Co–Fe–Cr multi-component system, it is difficult to obtain the bulk free energy density function  $f(c)$  due to the absence of the thermodynamic data. Actually, this system could be regarded as a pseudo-binary system of Al–TM since there exhibit strong interactions between Al and these transition metals TMs and weak interactions among TMs [22]. Thus, the  $f(c)$  would be expressed with a simple ‘double well’ potential given in Eq. (4) in a binary phase separating system [54,55]:

$$f(c) = Ac^2(1 - c)^2 \quad (4)$$

It characterizes an energy barrier between two equilibrium phases, the matrix BCC phase and the precipitated B2 phase, as presented in Fig. 1, in which the composition values of  $c = 0$  and  $c = 1.0$  correspond to the BCC matrix and B2 phase, respectively.  $A$  is a positive constant and controls the magnitude of the energy barrier between two equilibrium phases, and it is generally assigned as  $A = 1$  after non-dimensionalization [51,54].

For the elastic contribution to the total free energy  $F^{\text{el}}$ , it is expressed with Eq. (5) in light of the classical Khachaturyan’s microelasticity theory [56,57]:

$$F^{\text{el}} = N_V \int_V f^{\text{el}} dV = N_V \int_V \frac{1}{2} \sigma_{ij}^{\text{el}} \varepsilon_{ij}^{\text{el}} dV \quad (5)$$

$$\varepsilon_{ij}^{\text{el}} = \varepsilon_{ij} - \varepsilon_{ij}^0 \quad (5a)$$

$$\varepsilon_{ij} = \frac{1}{2} \left( \frac{\partial u_i}{\partial r_j} + \frac{\partial u_j}{\partial r_i} \right) \quad (5b)$$

$$\varepsilon_{ij}^0 = \beta(c) \varepsilon \delta_{ij} = \begin{pmatrix} \beta(c)\varepsilon & 0 & 0 \\ 0 & \beta(c)\varepsilon & 0 \\ 0 & 0 & \beta(c)\varepsilon \end{pmatrix} \quad (5c)$$

$$\beta(c) = c^3(10 - 15c + 6c^2) \quad (5d)$$

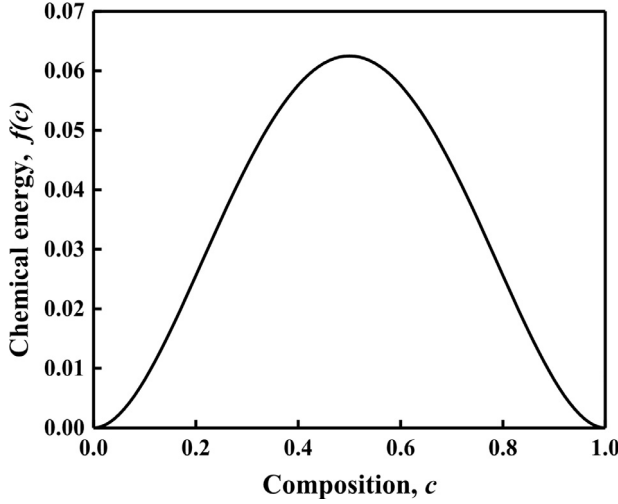


**Fig. 1.** Variation of chemical free energy  $f(c)$  as a function of the scaled composition  $c$ .

where  $f^{el}$  is the elastic energy density,  $\sigma_{ij}^{el}$  and  $\varepsilon_{ij}^{el}$  are the elastic stress and elastic strain, respectively. Particularly, the elastic strain  $\varepsilon_{ij}^{el}$  could be obtained by Eq. (5a), in which  $\varepsilon_{ij}$  is the total strain expressed with the displacement field variables of  $u_i$  and  $u_j$ , given by Eq. (5b).  $\varepsilon_{ij}^0$  is the eigenstrain (i.e. the intrinsic elastic strain), which is closely related to the lattice misfit  $\varepsilon$  between the precipitated phase and the matrix, as presented in Eq. (5c).  $\delta_{ij}$  is the Kronecker delta, and  $\beta(c)$  is an interpolation function of the composition  $c$  (Eq. (5d)) [58]. Here, it is assumed that both the matrix and precipitated phases keep a linear elastic theory, i.e., the Hooke's law relates the elastic stress to the elastic strain with Eq. (6) [56,57].

$$\sigma_{kl}^{el} = C_{ijkl}\varepsilon_{ij}^{el} \quad (6)$$

$$C_{ijkl} = C_{ijkl}^{eff} + \alpha(c)\Delta C_{ijkl} \quad (6a)$$

$$C_{ijkl}^{eff} = \frac{1}{2}(C_{ijkl}^m + C_{ijkl}^p) \quad (6b)$$

$$\Delta C_{ijkl} = C_{ijkl}^p - C_{ijkl}^m \quad (6c)$$

$$\alpha(c) = c^3(10 - 15c + 6c^2) - \frac{1}{2} \quad (6d)$$

where the  $C_{ijkl}$  is the elastic modulus tensor and is a function of the composition  $c$ , as seen in Eq. (6a). Among them, the effective elastic modulus  $C_{ijkl}^{eff}$  could be given by the arithmetic mean of two equilibrium phases (Eq. (6b)), in which the  $C_{ijkl}^m$  and  $C_{ijkl}^p$  represent the elastic modulus tensor of the matrix and the precipitated phase, respectively; and the  $\Delta C_{ijkl}$  is the modulus tensor difference between these two phases (Eq. (6c)). Moreover, the  $\alpha(c)$  is also a scalar interpolation function of the composition  $c$  (Eq. (6d)) [58], similar to the  $\beta(c)$ .

## 2.2. Non-dimensionalization

It is noted that all the parameters used in the present simulations are non-dimensional. However, the experimental data are dimensional, and it is necessary to dimensionize the simulation data for comparison with the experimental results. Therefore, we carried out the non-dimensionalization by using the characteristic length  $L'$ , time  $T'$ , and energy  $E'$ , in which the prime represents

that these quantities are dimensional. Thus, these three characteristic parameters could be obtained by the following series of operations (Eqs. (7a~7e)) [51,53]:

$$L' = \left( \frac{\kappa'}{A'} \right)^{\frac{1}{2}} \quad (7a)$$

$$T' = \frac{(c_p' - c_m')^2 L'^2}{M'E'} \quad (7b)$$

$$E' = \frac{3a^3\gamma'}{2L'} = A' \quad (7c)$$

$$t = \frac{t'}{T'} \quad (7d)$$

$$M' = \frac{(c_p' - c_m')^2}{2A'} D' \quad (7e)$$

where, all of these parameters without and with prime represent the nondimensional and dimensional parameters, respectively. By setting the characteristic length  $L' = 1$  nm in the simulation, the characteristic energy  $E'$  is calculated with Eq. (7c), being  $E' = 4.4 \times 10^{-21}$  J, in which the average lattice constant in the present BCC/B2 system is  $a = 0.287$  nm, and the interfacial energy between BCC and B2 phases is taken as  $\gamma' = 0.125$  J/m<sup>2</sup> [59]. Then the mobility  $M'$  could be obtained with Eq. (7e), being  $M' = 1096.7$  m<sup>2</sup>/(J·s), in which the experimental composition difference of the solute Al content in BCC and B2 is  $c_p' - c_m' = 0.35$  [22], and the interdiffusion coefficient of  $D' = 1.26 \times 10^{-16}$  m<sup>2</sup>/s is referred from that in BCC-Fe alloy steels [60]. Finally, the characteristic time step for the simulation could be calculated as  $T' = 0.02$  s. Moreover, the non-dimensional parameters of  $\kappa = 1$ ,  $A = 1$  and  $M = 1$  are assigned during the simulation. And the non-dimensional elastic modulus tensor  $C_{ijkl}^*$  is expressed with  $C_{ijkl}^* = C_{ijkl} / N_V$ , where  $N_V = 2 \times L'^3/a^3$ .

## 2.3. Computational solution

To simulate the coherent BCC/B2 microstructures and their microstructural evolution in Al-TM HEAs, we will solve the Cahn-Hilliard equation with the finite element method [54,61,62], which is executed by the partial differential equation (PDE) module and the solid mechanics module in COMSOL Multiphysics software [61]. The PDE module provides a general interface for specifying and solving PDEs in the general form, which is closely coupled with the conservation laws in many areas of physics. The solid mechanics module is applied to solve the elastic energy. Assuming that we are working with a single dependent variable  $u$ , the general form read in the COMSOL Multiphysics software is  $e_a \frac{\partial^2 u}{\partial t^2} + d_a \frac{\partial u}{\partial t} + \nabla \cdot \Gamma = f$  [63]. Thus, the Cahn-Hilliard equation (Eq. (2)) can be transformed into the general PDE form when an auxiliary variable  $\Psi$  is introduced, as seen in Eq. (8), where the  $\Psi$  is expressed by the partial derivative of the Eqs. (2, 3, and 5).

$$\begin{cases} \frac{\partial c(t,x)}{\partial t} - \nabla \cdot M \nabla \Psi = 0 \\ \nabla \cdot 2K \nabla c = \frac{\partial f(c)}{\partial c} - \Psi + \frac{\partial f^{el}}{\partial c} \end{cases} \quad (8)$$

Through comparing Eq. (8) with the general form of PDE in COMSOL Multiphysics [61], these parameters of  $e_a$ ,  $d_a$ ,  $\Gamma$  and  $f$ , could be rewritten with the expressions in Eqs. (8a~8d).

$$e_a = \begin{pmatrix} 0 & 0 \\ 0 & 0 \end{pmatrix} \quad (8a)$$

$$d_a = \begin{pmatrix} 1 & 0 \\ 0 & 0 \end{pmatrix} \quad (8b)$$

**Table 1**

Data summary for Al-TM HEAs, including chemical composition (at.%)<sup>a</sup>, lattice constants ( $a$ ) and lattice misfit ( $\varepsilon$ ) of BCC and B2 phases, as well as the volume fraction  $f$  and particle size  $d$  of precipitates.

No.	Chemical compositions (at.%)	$a_{B2}$ (nm)	$a_{BCC}$ (nm)	$\varepsilon$ (%)	$f$ (%)	$d$ (nm)
No.1-Al21	Al <sub>21.2</sub> Ni <sub>29.9</sub> Co <sub>21.1</sub> Fe <sub>13.8</sub> Cr <sub>14.0</sub>	0.2878 ± 0.0001	0.2875 ± 0.0001	0.1 ± 0.1	40	17 ~ 23
No.2-Al12	Al <sub>12.5</sub> Ni <sub>17.5</sub> Co <sub>17.5</sub> Fe <sub>17.5</sub> Cr <sub>35.0</sub>	0.2869 ± 0.0006	0.2856 ± 0.0003	0.5 ± 0.1	55	50 ~ 60
No.3-Al17	Al <sub>17.6</sub> Ni <sub>20.6</sub> Co <sub>20.6</sub> Fe <sub>20.6</sub> Cr <sub>20.6</sub>	0.2884 ± 0.0005	0.2866 ± 0.0004	0.7 ± 0.2	50	—

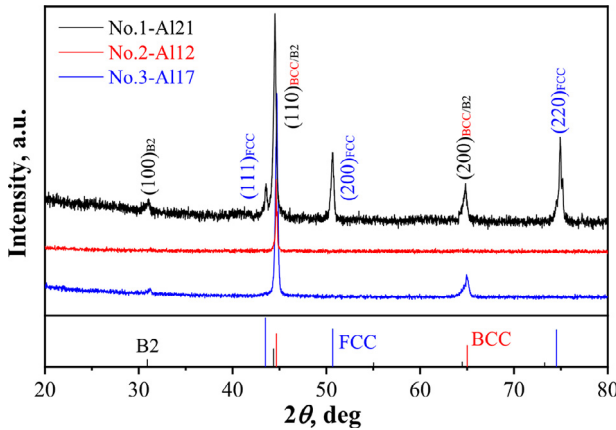


**Fig. 2.** XRD patterns of as-cast Al-TM HEAs, Al<sub>21.2</sub>Ni<sub>29.9</sub>Co<sub>21.1</sub>Fe<sub>13.8</sub>Cr<sub>14.0</sub> (No.1-Al21), Al<sub>12.5</sub>Ni<sub>17.5</sub>Co<sub>17.5</sub>Fe<sub>17.5</sub>Cr<sub>35.0</sub> (No.2-Al12), and Al<sub>17.6</sub>Ni<sub>20.6</sub>Co<sub>20.6</sub>Fe<sub>20.6</sub>Cr<sub>20.6</sub> (No.3-Al17).

$$\Gamma = \begin{pmatrix} -M \frac{\partial \Psi}{\partial x} & -M \frac{\partial \Psi}{\partial y} \\ \kappa \frac{\partial c}{\partial x} & \kappa \frac{\partial c}{\partial y} \end{pmatrix} \quad (8c)$$

$$f = \begin{pmatrix} 0 \\ \frac{\partial f(c)}{\partial c} - \Psi + \frac{\partial f^{el}}{\partial c} \end{pmatrix} \quad (8d)$$

### 3. Experimental

Three BCC/B2-based Al-Ni-Co-Fe-Cr HEAs were taken to investigate the particle morphologies of precipitates, where the alloy compositions in atomic percent (at.%) are listed in Table 1, named as No.1-Al21, No.2-Al12, and No.3-Al17, respectively. These HEAs were prepared by the arc melting and copper-mold suction cast method under an argon atmosphere, which was described particularly in our previous work [16]. Crystalline structures of these suction-cast alloys were identified using a Bruker D8 X-ray diffractometer (XRD) with the Cu- $K_\alpha$  radiation ( $\lambda = 0.15406$  nm), in which the lattice constants of BCC and B2 phases could be obtained for the calculation of the lattice misfit  $\varepsilon$ . The microstructures (especially the particle morphologies) were examined using Olympus optical microscopy (OM), Zeiss Supra 55 scanning electron microscopy (SEM), and JEOL-JEM-2100F field emission transmission electron microscopy (TEM). The etching solution for OM and SEM observation was composed of 5 g FeCl<sub>3</sub>·6H<sub>2</sub>O + 25 ml HCl + 25 ml C<sub>2</sub>H<sub>5</sub>OH, and the TEM specimens were prepared by twin-jet electro-polishing in a solution of 10% HClO<sub>4</sub> + 90% C<sub>2</sub>H<sub>5</sub>OH (volume fraction) below a cryogenic temperature of 243 K.

## 4. Results

### 4.1. Experimental microstructural characterization

The XRD patterns of these three Al-TM HEAs are shown in Fig. 2, from which it was found that both No.2-Al12 (Al<sub>12.5</sub>Ni<sub>17.5</sub>Co<sub>17.5</sub>Fe<sub>17.5</sub>Cr<sub>35.0</sub>) and No.3-Al17 (Al<sub>17.6</sub>Ni<sub>20.6</sub>Co<sub>20.6</sub>Fe<sub>20.6</sub>Cr<sub>20.6</sub>) alloys are composed of the BCC solid solution and the ordered B2 phase (characterized by a weak (100)

diffraction peak). For the No.1-Al21 (Al<sub>21.2</sub>Ni<sub>29.9</sub>Co<sub>21.1</sub>Fe<sub>13.8</sub>Cr<sub>14.0</sub>) alloy, there still exists a small amount of FCC phase, besides the BCC and B2 phases. The lattice constants of BCC and B2 phases,  $a_{BCC}$  and  $a_{B2}$ , in these HEAs were measured and generalized in Table 1. Then the lattice misfit  $\varepsilon$  between the BCC and B2 could be calculated with the expression of  $\varepsilon = 2 \times (a_{B2} - a_{BCC}) / (a_{B2} + a_{BCC})$ , and these values are also listed in Table 1.

The detailed microstructures of these three as-cast Al-TM HEAs are shown in Fig. 3. The OM observations (Fig. 3(a)) show that the No.1-Al21 alloy is constituted of the primary dark BCC/B2 dendrites plus the bright FCC phase in the inter-dendrites. While the coarse columnar dendritic microstructure appears in both No.2-Al12 and No.3-Al17 alloys (Fig. 3(c, e)), which is much more obviously in No.2-Al12, resulting in some preferred orientation that demonstrated by the XRD analysis. The precipitate morphologies were characterized by both SEM observations (the insets in Fig. 3(a, c, e)) and TEM analysis (Fig. 3(b, d, f)). For the BCC/B2 dendrites in No.1-Al21, the TEM dark-field (DF) image and selected-area electronic diffraction (SAED) pattern demonstrate that the spherical BCC nanoparticles with a size of about 17 ~ 23 nm are precipitated in the B2 matrix, as shown in Fig. 3(b), which is consistent with the SEM observation (the inset in Fig. 3(a)). On the contrary, for the No.2-Al12 alloy, the matrix exhibits a BCC solid solution structure, and the B2 nanoprecipitates are in a cuboidal shape with a particle size of about 50 ~ 60 nm (Fig. 3(d)). Different from both the spherical and cuboidal precipitates in the above two alloys, a weave-like spinodal decomposition microstructure is formed in No.3-Al17 alloy, as seen in Figs. 3(e, f). Actually, our previous work has generalized that the diverse coherent microstructures in Al-Ni-Co-Fe-Cr system are primarily dependent on the lattice misfit  $\varepsilon$  between BCC and B2 phases [22]. A small  $\varepsilon$  ( $\varepsilon < 0.2\%$ ) generally corresponds to a precipitation of small-sized spherical/ellipsoidal nanoparticles, and a moderate  $\varepsilon$  ( $\varepsilon \sim 0.4\%$ ) can result in a precipitation of cuboidal nanoparticles with a relatively larger size, while a much large  $\varepsilon$  ( $\varepsilon > 0.6\%$ ) would lead to a weave-like spinodal decomposition microstructure [22]. The  $\varepsilon$  values of the present three HEAs are 0.1%, 0.5%, and 0.7%, respectively, as a result of the formations of spherical, cuboidal nanoprecipitates and a weave-like microstructure. Moreover, the volume fractions ( $f$ ) of precipitates in No.1 and No.2 alloys were measured, being 40% and 55%, respectively. It is noted that the volume fraction of BCC particles in No.1 alloy is only calculated in the BCC/B2 dendrites for the following simulation. For the No.3 alloy with the weave-like microstructure, the BCC and B2 phases are evenly distributed, i.e., the volume fraction of B2 is about 50%.

### 4.2. Simulation results

All the parameters used in the simulations of these three alloys are listed in Table 2, including the Cahn-Hilliard model [47,48,54], lattice misfit  $\varepsilon$ , and elastic modulus tensors for these alloys. The evolution of the coherent microstructure is simulated by given concentration field variables, elastic modulus tensors of the BCC and ordered B2 phases and lattice misfit between these two phases. Fig. 4 shows the phase-field simulation results of these three HEAs with different coherent microstructures, in which the two-dimensional domain boundaries are periodic in every direc-

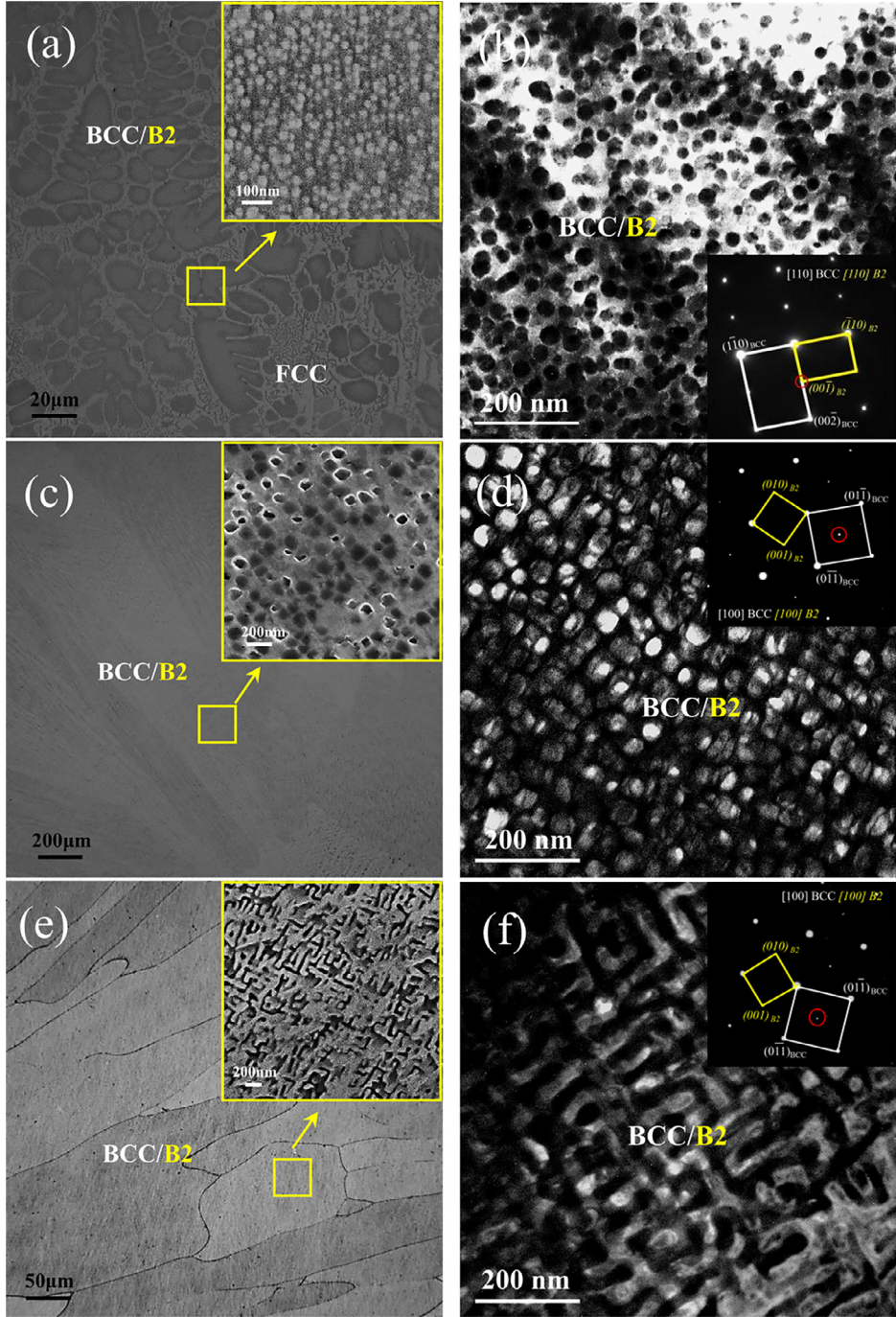


**Fig. 3.** Microstructural morphologies of as-cast Al-TM HEAs. (a, b):  $\text{Al}_{21.2}\text{Ni}_{29.9}\text{Co}_{21.1}\text{Fe}_{13.8}\text{Cr}_{14.0}$  (No.1-Al21), in which the dark-field TEM image (b) of the BCC/B2 region shows that BCC particles are embedded in the B2 matrix; (c, d):  $\text{Al}_{12.5}\text{Ni}_{17.5}\text{Co}_{17.5}\text{Fe}_{17.5}\text{Cr}_{35.0}$  (No.2-Al12), in which the cuboidal B2 nanoparticles in BCC matrix are identified by the dark-field TEM analysis (d); (e, f):  $\text{Al}_{17.6}\text{Ni}_{20.6}\text{Co}_{20.6}\text{Fe}_{20.6}\text{Cr}_{20.6}$  (No.3-Al17), in which the BCC/B2 coherent microstructure shows a weave-like morphology.

tion with the number of grid points of  $N_x = N_y = 500$  and the grid spacing of  $\Delta x = \Delta y = 1 \text{ nm}$ , and the blue and red areas represent the BCC and the ordered B2 phases, respectively. It is found that in the No.1-Al21 alloy with a smaller lattice misfit of  $\varepsilon = 0.1\%$ , the BCC nanoparticles with the size of about  $20 \sim 36 \text{ nm}$  exhibit both spherical and ellipsoidal shapes, i.e., the small-sized particles are spherical and the large-sized are ellipsoidal (Fig. 4(a)). Increasing the lattice misfit to  $\varepsilon = 0.5\%$  of the No.2-Al12 alloy (Fig. 4(b)), the morphology of B2nanoprecipitates exhibits a cuboidal shape, and the particle size is about  $32 \sim 50 \text{ nm}$ . When the lattice misfit is further enhanced up to  $\varepsilon = 0.7\%$  in No.3-Al17 alloy, a typical weave-like microstructure could be obtained through the simula-

tion, as shown in Fig. 4(c). By comparison, the simulation results of coherent microstructures are well consistent with the experimental results (Fig. 3).

In order to understand the coarsening process of nanoprecipitates, we extended the time step to  $t = 20,000$  in the simulation. Fig. 5 shows the simulated coarsening process of nanoprecipitates in these three HEAs, in which the time step is taken as  $t = 1000, 5000, 10,000, 15,000$ , and  $20,000$ , respectively. For the spherical or ellipsoidal precipitation (Fig. 5(a1–a5)), the precipitated particles are much smaller at an initial stage ( $t = 1000$ ), in which the particle size is about  $12 \sim 20 \text{ nm}$ . Extending the time step to  $t = 20,000$ , the particle size increases to  $36 \sim 57 \text{ nm}$ . While in the No.2-Al12

**Table 2**

Parameters used in the phase-field simulations.  $M$ : mobility;  $\kappa$ : gradient energy coefficient;  $A$ : energy barrier;  $\varepsilon$  : lattice misfit between BCC and B2 phases;  $C_{11}$ ,  $C_{12}$  and  $C_{44}$ : elastic modulus tensor;  $\Delta x$  and  $\Delta y$ : unit length of simulated meshes; and  $\Delta t$ : unit time step.

Parameter type	Parameter	Value used
Cahn–Hilliard model [47]	$M$	1.0
	$\kappa$	1.0
	$A$	1.0
Lattice misfit	$\varepsilon$	0.1% (for ellipsoidal precipitates) 0.5% (for cuboidal precipitates) 0.7% (for weave-like microstructure)
	BCC	$C_{11}/N_V$ $C_{12}/N_V$ $C_{44}/N_V$
	B2	$C_{11}/N_V$ $C_{12}/N_V$ $C_{44}/N_V$
Simulation	$\Delta x$	603
	$\Delta y$	339
	$\Delta t$	304
Elastic modulus tensor	BCC	621
	B2	323
		304
Simulation	$\Delta x$	1.0
	$\Delta y$	1.0
	$\Delta t$	1.0

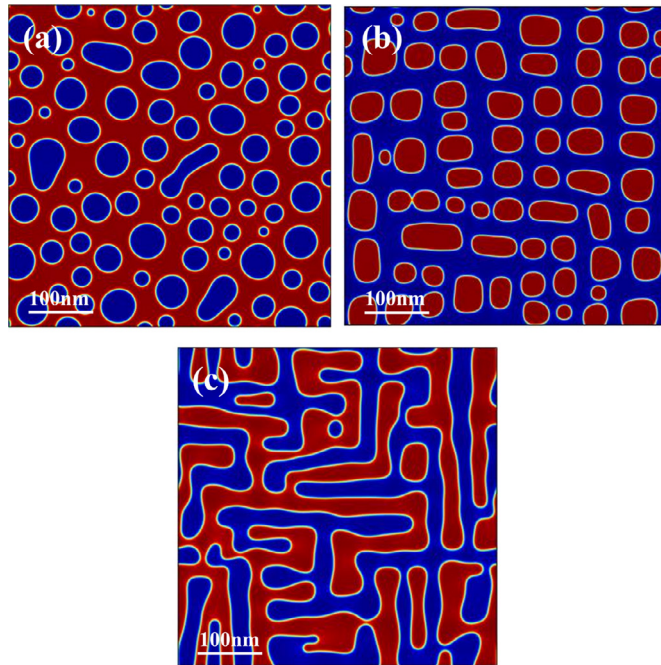


**Fig. 4.** Simulated microstructures in Al-TM HEAs by phase field method at the time step of  $t = 10,000$ . (a): No.1-Al21, (b): No.2-Al12, and (c): No.3-Al17, in which the blue and red zones represent the BCC phase and ordered B2 phase, respectively. The volume fraction of precipitated phase is 40%, 55%, and 50%, respectively. (For interpretation of the references to colour in this figure legend, the reader is referred to the web version of this article.)

alloy with  $\varepsilon = 0.5\%$ , the particle morphology exhibits a spherical or a short-rod shape at the initial stage with  $t = 1000$  (Fig. 5(b1)), and two spherical particles could be emerged into a larger ellipsoidal one with extending the time to  $t = 5000$  (Fig. 5(b2)). When the time is further extended to  $t = 10,000 \sim 20,000$  (Figs. 5(b3–b5)), the ellipsoidal particles are being regulated and most of these particles would be changed into the cuboids with a size of about 35 ~ 60 nm. It is noted that the particle size of most cuboidal precipitates keeps almost constant with the time increase from  $t = 10,000$  to  $t = 20,000$ . In addition, this morphology evolution of nanoprecipitates in the No.2-Al12 is different from that in No.1-Al21, which is evidenced by the fact that there is no change in the particle morphology in the No.1-Al21 alloy with a smaller  $\varepsilon$ . For the weave-like spinodal decomposition microstructure in the No.3-Al17 alloy, the

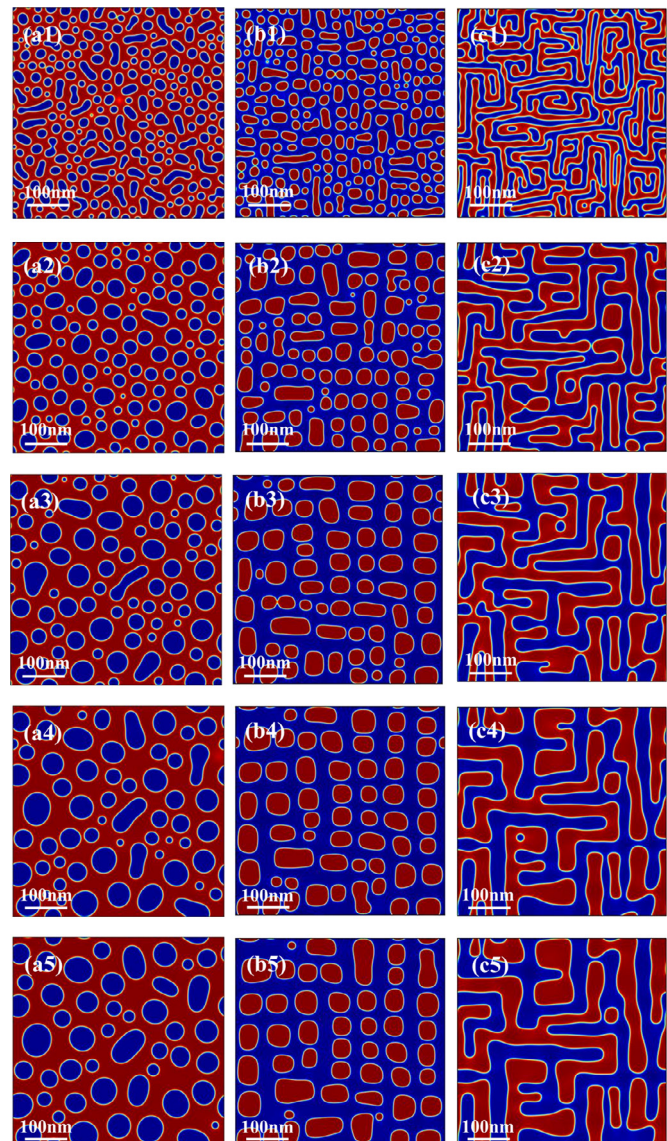


**Fig. 5.** Simulated results for microstructural evolution in Al-TM HEAs at different time steps of  $t = 1000$  (1), 5000 (2), 10,000 (3), 15,000 (4), and 20,000 (5). (a): No.1-Al21, (b): No.2-Al12, and (c): No.3-Al17, in which the blue and red zones represent the BCC phase and ordered B2 phase, respectively. (For interpretation of the references to colour in this figure legend, the reader is referred to the web version of this article.)

width of spinodal decomposition increases gradually from the 10 ~ 16 nm at  $t = 1000$  to 24 ~ 45 nm at  $t = 20,000$ , during which no change occurs in the morphology.

## 5. Discussion

### 5.1. Effect of the anisotropy of Young's modulus on the morphology of precipitated particles

Through the simulations, it was found that the morphology of precipitated particles is not only controlled by the lattice misfit  $\varepsilon$ , but also related to the anisotropy of Young's modulus of BCC and B2 phases. For spherical particles, the lattice misfit plays a dominant role, while the effect of the anisotropy could be neglected. However, when the lattice misfit is relatively large to form cuboidal nanoprecipitates or a weave-like spinodal decomposition, the influence of the anisotropy is particularly important. Especially,

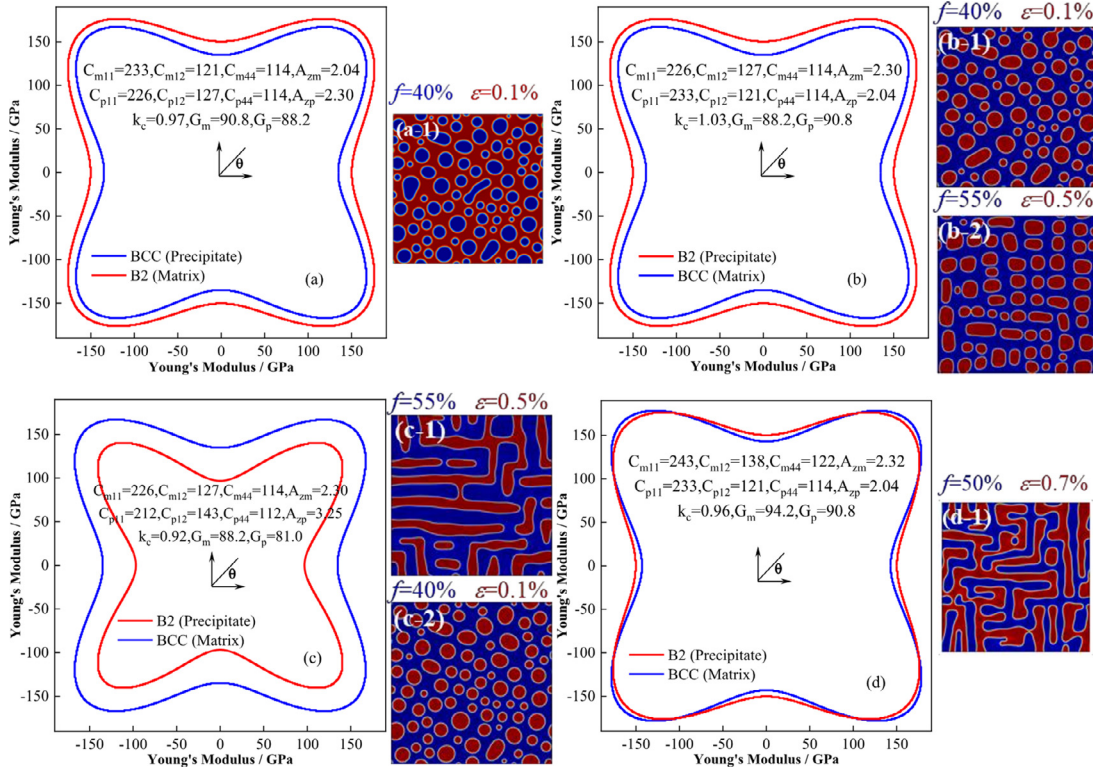


**Fig. 6.** Direction distribution functions of Young's modulus in Al-TM HEAs (a-d), in which the blue and red lines represent the BCC phase and B2 phase, respectively;  $\theta$  is the angle with respect to the elastic main axis; (a-1) ~ (d-1) are the corresponding simulated results of microstructures. (For interpretation of the references to colour in this figure legend, the reader is referred to the web version of this article.)

the cuboidal shape of nan precipitates is very sensitive to the anisotropy of Young's modulus, in which  $A_z$  is the Zener-anisotropy ratio [64] and  $G$  is the shear modulus given by Eqs. (9) and (10):

$$A_z = \frac{2C_{44}}{C_{11} - C_{12}} \quad (9)$$

$$G = \frac{3C_{44} + C_{11} - C_{12}}{5} \quad (10)$$

where  $C_{11}$ ,  $C_{12}$  and  $C_{44}$  are elastic modulus tensors. In Al-TM HEAs, the ordered B2 phase is always segregated by Ni and Al elements alone, while the BCC solid solution phase is enriched by the Fe, Co, and Cr elements [16]. For instance, in No.2-Al12 alloy with cuboidal B2 nan precipitates, the elastic modulus tensors of B2 phase are determined as  $C_{11} = 233$  GPa,  $C_{12} = 121$  GPa, and  $C_{44} = 114$  GPa, respectively, which are taken from the calculated values by the first principles simulation [65], resulting in a shear modulus of  $G_{B2} = 90.8$  GPa. The elastic modulus tensors of the BCC matrix are taken as  $C_{11} = 226$  GPa,  $C_{12} = 127$  GPa, and  $C_{44} = 114$  GPa, respectively, which are the values of the BCC Fe-35Cr-15Co alloy ( $G = 88.2$  GPa) [66]. Then we define a parameter of  $k_c = G^p / G^m$  to compare the shear modulus of the precipitate phase ( $G^p$ ) and the matrix ( $G^m$ ).

For cubic systems, the Young's modulus  $E(\theta)$  as a function of direction is given by:

$$E(\theta) = \left( \frac{C_{11} + C_{12}}{(C_{11} - C_{12})(C_{11} + 2C_{12})} - \frac{1 - \cos(4\theta)}{4} \left( \frac{1}{C_{11} - C_{12}} - \frac{1}{2C_{44}} \right) \right)^{-1} \quad (11)$$

where  $\theta$  is the angle with respect to the elastic main axis [67]. In order to investigate the effect of the  $E$  anisotropy on the particle morphology, the direction distribution functions of Young's modulus  $E(\theta)$  in Al-TM HEA systems obtained from the embedded matplotlib extended library of the Jupyter notebook [68] through

Eqs. (9-11) are shown in Fig. 6. For the No.2-Al12 HEA, the direction distribution functions of Young's modulus of the precipitated B2 phase is outside of that of the BCC matrix phase (Fig. 6(b)), which would result in the  $k_c$  value ( $k_c = 1.03$ ) slightly larger than 1.0, i.e., the shear modulus of the precipitated B2 phase is larger than that of the BCC matrix phase. Under this case, the precipitation of cuboidal B2 particles could occur only when the lattice misfit reaches a moderate value, such as  $\varepsilon = 0.5\%$  (Fig. 6(b-2), with  $f = 55\%$ ). Otherwise, spherical B2 nan precipitates appear in the BCC matrix when the lattice misfit decreases to  $\varepsilon = 0.1\%$  while the elastic tensors are not changed, as seen in Fig. 6(b-1). If the precipitated phase and the matrix are inverted, but the elastic modulus tensors of these two phases keep same to those taken in Fig. 2(b), then the direction distribution functions of Young's modulus of the precipitated BCC phase would be inside of that of the B2 matrix, which is taken in the microstructural simulation of No.1-Al21 alloy. Spherical BCC nan precipitates would appear with  $\varepsilon = 0.1\%$  and  $f = 40\%$  (Fig. 6(a-1)). Therefore, whatever the nan precipitates exhibit a BCC or B2 structure, the particle shape is always spherical, which indicates that the particle morphology is non-sensitive to the anisotropy of Young's modulus, but is dependent on the lattice misfit alone.

On the other side, if we adjusted the elastic modulus tensors of precipitated B2 phase, as  $C_{11} = 212$  GPa,  $C_{12} = 143$  GPa,  $C_{44} = 112$  GPa, and  $G = 81$  GPa, which are taken from the experimental values of the B2-NiAl phase [69], the direction distribution functions of Young's modulus of B2 would be inside of that of the BCC matrix (Fig. 6(c)). In this case, the  $k_c$  value ( $k_c = 0.92$ ) is smaller than 1.0, i.e., the shear modulus of the B2 is smaller than that of the BCC. Thus, a weave-like microstructure will be formed at  $\varepsilon = 0.5\%$  and  $f = 55\%$ , as seen in Fig. 6(c-1). However, keeping the volume fraction of  $f = 40\%$  and a smaller lattice misfit of  $\varepsilon = 0.1\%$  will correspond to a coherent microstructure with spherical or ellipsoidal B2 nan precipitates in the same condition

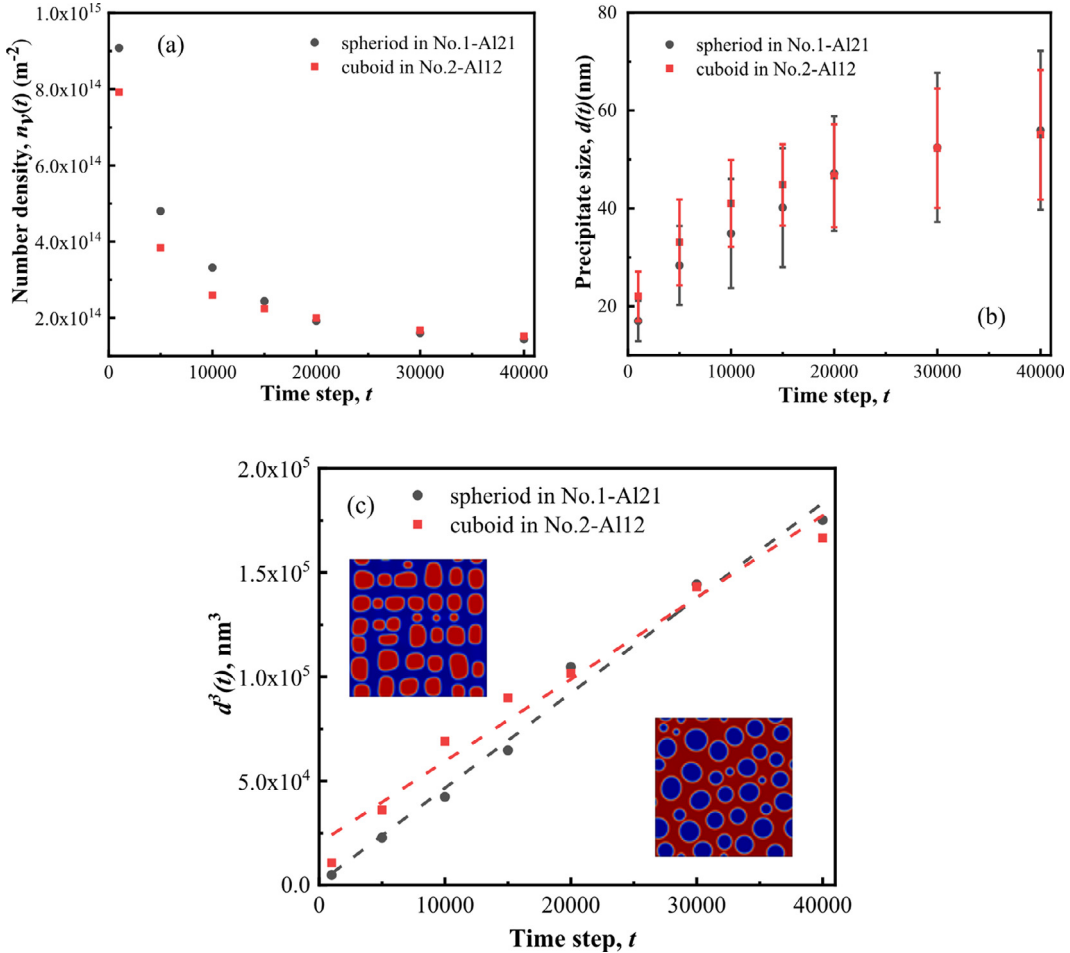


**Fig. 7.** Variations of number density of precipitates (a) and precipitate size ( $d(t)$ ) (b) and  $d^3(t)$  (c) versus the time step from  $t = 1000$  to  $t = 40,000$  in phase-field simulation, in which the black points and red points represent spherical and cuboidal precipitates in  $\text{Al}_{21.2}\text{Ni}_{29.9}\text{Co}_{21.1}\text{Fe}_{13.8}\text{Cr}_{14.0}$  (No.1-Al21) and  $\text{Al}_{12.5}\text{Ni}_{17.5}\text{Co}_{17.5}\text{Fe}_{17.5}\text{Cr}_{35.0}$  (No.2-Al12) HEAs, respectively. (For interpretation of the references to colour in this figure legend, the reader is referred to the web version of this article.)

(Fig. 6(c-2)). All of these simulation results demonstrate that the cuboidal nanoprecipitation is controlled by both the lattice misfit and the anisotropy of Young's moduli of the precipitated phase and the matrix. While the spherical nanoprecipitation is primarily related to the former.

In fact, the elastic modulus tensors of both BCC and B2 phases could vary with alloy compositions in different HEAs. For the weave-like spinodal decomposition like in No.3-Al17 alloy, it is found that when the direction distribution functions of Young's modulus of B2 is overlapped with that of the BCC matrix (Fig. 6(d)), the simulation result could be consistent well with the experimental microstructure (Fig. 3(f) and Fig. 6(d-1)). In this case, the elastic modulus tensors of the BCC matrix are changed to be  $C_{11} = 243 \text{ GPa}$ ,  $C_{12} = 138 \text{ GPa}$ , and  $C_{44} = 122 \text{ GPa}$  taken from pure Fe ( $G = 94.2 \text{ GPa}$ ) [70], compared with those data taken in Fig. 6(a). Although these elastic modulus tensors of BCC and B2 phases are gathered from the existing data, the diverse combinations of these values could reflect the coherent microstructural evolution obviously in the simulations.

## 5.2. Coarsening behavior of precipitated particles

The classical Lifshitz-Slyozov-Wanger (LSW) theory has been developed to describe the coarsening behavior of precipitated particles in dilute alloy systems, in which the average precipitate size  $d$  is proportional to the cubic root of the annealing time  $t$ ,  $d \propto t^{1/3}$  [71]. According to this theory, the conventional coarsening phe-

nomenon is caused by the decrease of interfacial energies of systems, i.e., small grains are dissolved, and large grains grow up, which is also called the Ostwald ripening. However, the LSW theory is based on isolated spherical precipitated particles, in which the volume fraction of the precipitates is approximately zero in the initial state and the effect of coherent strain on the coarsening is also neglected. In practical multicomponent solid-solution alloy systems, the volume fraction of the precipitate phase is always more than 30%, and the crystal structure will be rearranged during the phase transformation. Consequently, an elastic stress field will be formed due to the lattice misfit between the precipitated phase and the matrix. In order to remove the restrictions of the LSW theory, it was extended to multi-component systems by Philippe and Voorhees (PV) [72]. According to the PV model, the coarsening behavior of precipitates could be expressed with Eq. (12) [73]:

$$d^3(t) - d^3(t_0) = K(t - t_0) \quad (12)$$

where  $K$  is the coarsening rate constant,  $d(t)$  is the average size at time  $t$ , and  $t_0$  refers to the time at the onset of coarsening.

We counted the number density and particle size of precipitates in No.1-Al21 and No.2-Al12 alloys at each time step of  $t = 1000 \sim 20,000$  in the simulation results (Fig. 5). In order to further investigate the coarsening tendency of precipitates, the simulation time was extended to  $t = 40,000$ . These statistics are shown in Fig. 7, in which the number density of precipitates (Fig. 7(a)) decreases but the particle size (Fig. 7(b)) increases obviously with the increase of the time from  $t = 1000$  to  $t = 20,000$ , indicating

that these nanoprecipitates are gradually coarsening. Then the tendency varies slowly when  $t > 20,000$ , as demonstrated by the fact that the particle size (40 ~ 72 nm) at  $t = 40,000$  is slightly larger than that at  $t = 20,000$  (Fig. 7(b)). In addition, the simulated microstructures of spherical and cuboidal precipitation at  $t = 40,000$  are also given in the inset of Fig. 7(b), which are comparable to their respective morphology at  $t = 20,000$ . It is emphasized that the driving force for particle coarsening is the decrease of the total bulk free energy, and the coarsening mechanism is the collision of adjacent particles to merge into larger particles. The variations of the average precipitate size ( $d^2(t)$ ) with the time step ( $t$ ) of No.1-Al21 and No.2-Al12 alloys are presented in Fig. 7(c), in which the average coarsening rate ( $K$ ) of precipitates could be fitted, being  $K = 228 \text{ nm}^3/\text{s}$  for spherical particles and  $K = 196 \text{ nm}^3/\text{s}$  for cuboidal particles, respectively. It indicates that the coarsening of spherical particles is relatively larger than that of the cuboidal particles. Particularly, the coarsening rate ( $K = 400 \text{ nm}^3/\text{s}$ ) of spherical particles at the stage of  $t = 15,000 \sim 2000$  is faster obviously than that ( $K = 119 \text{ nm}^3/\text{s}$ ) of cuboidal particles, after which the particle size of the former is comparable to that of the latter. It could indicate that the coherent microstructure with cuboidal precipitation exhibits a much higher microstructural stability.

## 6. Conclusions

In this study, the phase-field method based on the Chan-Hilliard equation was taken to simulate the evolutions of coherent BCC/B2 microstructures in Al-Ni-Co-Fe-Cr HEAs using the COMSOL Multiphysics software. The coherent microstructures include the spherical precipitation, cuboidal precipitation, and weave-like spinodal decomposition, which were obtained in the present experiments. The simulated results on these three typical microstructures are well consistent with the experiments. It was found that both the lattice misfit and the anisotropy difference of Young's moduli between the precipitated phase and matrix phase affect the morphology of precipitates. In particular, the coherent microstructure with cuboidal nanoprecipitation is sensitive to the modulus anisotropy on the premise of a moderate lattice misfit ( $\varepsilon \sim 0.5\%$ ), while the spherical precipitation is mainly controlled by a small lattice misfit ( $\varepsilon \sim 0.1\%$ ). During the coarsening process of precipitates in the simulations, it was found that the coarsening rate of spherical particles is relatively larger than that of cuboidal particles, which means that the coherent microstructure with cuboidal precipitation would exhibit a much higher stability.

## Declaration of Competing Interest

The authors declare that they have no known competing financial interests or personal relationships that could have appeared to influence the work reported in this paper.

## Acknowledgements

It was supported by the National Natural Science Foundation of China [No. 91860108 and U1867201], the National Key Research and Development Plan (2017YFB0702401), Natural Science Foundation of Liaoning Province of China (No. 2019-KF-05-01), and the Fundamental Research Funds for the Central Universities (DUT19LAB01).

## References

- [1] M.A. Meyers, K.K. Chawla, *Mechanical Behavior of Materials*, 2nd edition, Cambridge University Press, Cambridge, UK, 2009.
- [2] H. Gleiter, E. Hornbogen, Precipitation hardening by coherent particles, *Mater. Sci. Eng. A* 6 (1968) 285–302.
- [3] R.C. Reed, *The Superalloys: Fundamentals and Applications*, Cambridge University Press, New York, USA, 2006.
- [4] X.G. Wang, J.L. Liu, T. Jin, X.F. Sun, The effects of ruthenium additions on tensile deformation mechanisms of single crystal superalloys at different temperatures, *Mater. Des.* 63 (2014) 286–293.
- [5] W.R. Wang, W.L. Wang, S.C. Wang, Y.C. Tsai, C.H. Lai, J.W. Yeh, Effects of Al addition on the microstructure and mechanical property of  $\text{Al}_x\text{CoCrFeNi}$  high-entropy alloys, *Intermetallics* 26 (2012) 44–51.
- [6] Y.F. Kao, T.J. Chen, S.K. Chen, J.W. Yeh, Microstructure and mechanical property of as-cast, -homogenized, and -deformed  $\text{Al}_x\text{CoCrFeNi}$  ( $0 \leq x \leq 2$ ) high-entropy alloys, *J. Alloys Compd.* 488 (2009) 57–64.
- [7] Z.K. Teng, M.K. Miller, G. Ghosh, C.T. Liu, S.Y. Huang, K.F. Russell, M.E. Fine, P.K. Liaw, Characterization of nanoscale NiAl-type precipitates in a ferritic steel by electron microscopy and atom probe tomography, *Scripta Mater.* 63 (2010) 61–64.
- [8] Z.Q. Sun, G. Song, J. Ilavsky, P.K. Liaw, Duplex precipitates and their effects on the room-temperature fracture behaviour of a NiAl-strengthened ferritic alloy, *Mater. Res. Lett.* 3 (2015) 128–134.
- [9] Z.K. Teng, C.T. Liu, G. Ghosh, P.K. Liaw, M.E. Fine, Effects of Al on the microstructure and ductility of NiAl-strengthened ferritic steels at room temperature, *Intermetallics* 18 (2010) 1437–1443.
- [10] M.J. Rawlings, C.H. Liebscher, M. Asta, D.C. Dunand, Effect of titanium additions upon microstructure and properties of precipitation-strengthened Fe-Ni-Al-Cr ferritic alloys, *Acta Mater.* 128 (2017) 103–112.
- [11] G. Song, Z.Q. Sun, L. Li, X.D. Xu, M. Rawlings, C.H. Liebscher, B. Clausen, J. Poplawsky, D.N. Leonard, S.Y. Huang, Z.K. Teng, C.T. Liu, M.D. Asta, Y.F. Gao, D.C. Dunand, G. Ghosh, M.W. Chen, M.E. Fine, P.K. Liaw, Ferritic alloys with extreme creep resistance via coherent hierarchical precipitates, *Sci. Rep.* 5 (2015) 16327.
- [12] H. Diao, X. Xie, F. Sun, K.A. Dahmen, P.K. Liaw, Mechanical properties of high-entropy alloys, in: M.C. Gao, J.W. Yeh, P.K. Liaw, Y. Zhang (Eds.), *High-entropy alloys: Fundamentals and Applications*, Springer, Berlin, 2016, pp. 181–236.
- [13] Y. Zhang, T.T. Zuo, Z. Tang, M.C. Gao, K.A. Dahmen, P.K. Liaw, Z.P. Lu, Microstructures and properties of high-entropy alloys, *Prog. Mater. Sci.* 61 (2014) 1–93.
- [14] Y. Zhang, Y.J. Zhou, J.P. Lin, G. Chen, P.K. Liaw, Solid-solution phase formation rules for multi-component alloys, *Adv. Eng. Mater.* 10 (2008) 534–538.
- [15] K.M. Youssef, A.J. Zaddach, C. Niu, D.L. Irving, C.C. Koch, A novel low-density, high-hardness, high-entropy alloy with close-packed single-phase nanocrystalline structures, *Mater. Res. Lett.* 2 (2014) 95–99.
- [16] Y. Ma, J.M. Hao, Q. Wang, C. Zhang, C.L. Li, C. Dong, Temperature-affected microstructural stability of coherent cuboidal B2 particles in precipitation-strengthened body-centered-cubic  $\text{Al}_{0.7}\text{CoCr}_2\text{FeNi}$  high-entropy alloy, *J. Mater. Sci.* 54 (2019) 8696–8710.
- [17] Z.Y. Lyu, X.S. Fan, C. Lee, S.Y. Wang, R. Feng, P.K. Liaw, Fundamental understanding of mechanical behavior of high-entropy alloys at low temperatures: a review, *J. Mater. Res.* 33 (2018) 2998–3010.
- [18] Y. Zou, Nanomechanical studies of high-entropy alloys, *J. Mater. Res.* 33 (2018) 3035–3054.
- [19] W.D. Li, G. Wang, S.W. Wu, P.K. Liaw, Creep, fatigue, and fracture behavior of high-entropy alloys, *J. Mater. Res.* 33 (2018) 3011–3034.
- [20] J.M. Hao, Y. Ma, Q. Wang, C. Zhang, C.L. Li, C. Dong, Q. Song, P.K. Liaw, Formation of cuboidal B2 nanoprecipitates and microstructural evolution in the body-centered-cubic  $\text{Al}_{0.7}\text{NiCoFe}_{1.5}\text{Cr}_{1.5}$  high-entropy alloy, *J. Alloys Compd.* 780 (2019) 408–421.
- [21] Q. Wang, Y. Ma, B.B. Jiang, X.N. Li, Y. Shi, C. Dong, P.K. Liaw, A cuboidal b2 nanoprecipitation-enhanced body-centered-cubic alloy  $\text{Al}_{0.7}\text{CoCr}_2\text{Fe}_2\text{Ni}$  with prominent tensile properties, *Scripta Mater.* 120 (2016) 85–89.
- [22] Y. Ma, Q. Wang, B.B. Jiang, C.L. Li, J.M. Hao, X.N. Li, C. Dong, T.G. Nieh, Controlled formation of coherent cuboidal nanoprecipitates in body-centered cubic high-entropy alloys based on  $\text{Al}_2(\text{NiCoFeCr})_{14}$  compositions, *Acta Mater.* 147 (2018) 213–225.
- [23] Y. Ma, B.B. Jiang, C.L. Li, Q. Wang, C. Dong, P.K. Liaw, F. Xu, L.X. Sun, The BCC/B2 morphologies in  $\text{Al}_x\text{NiCoFeCr}$  high-entropy alloys, *Metals (Basel)* 7 (2017) 57–68.
- [24] S. Kolling, D. Gross, Simulation of microstructural evolution in materials with misfitting precipitates, *Probabilistic Eng. Mech.* 16 (2001) 313–322.
- [25] V. Vaithyanathan, L.Q. Chen, Coarsening of ordered intermetallic precipitates with coherency stress, *Acta Mater.* 50 (2002) 4061–4073.
- [26] J.Z. Zhu, Z.K. Liu, V. Vaithyanathan, L.Q. Chen, Linking phase-field model to CALPHAD: application to precipitate shape evolution in Ni-base alloys, *Scripta Mater.* 46 (2002) 401–406.
- [27] Y.H. Wen, J.P. Simmons, C. Shen, C. Woodward, Y. Wang, Phase-field modeling of bimodal particle size distributions during continuous cooling, *Acta Mater.* 51 (2003) 1123–1132.
- [28] J.Z. Zhu, T. Wang, A.J. Ardell, S.H. Zhou, Z.K. Liu, L.Q. Chen, Three-dimensional phase-field simulations of coarsening kinetics of  $\gamma'$  particles in binary Ni-Al alloys, *Acta Mater.* 52 (2004) 2837–2845.
- [29] Y.H. Wen, B. Wang, J.P. Simmons, Y. Wang, A phase-field model for heat treatment applications in Ni-based alloys, *Acta Mater.* 54 (2006) 2087–2099.
- [30] J.C. Wang, M. Osawa, T. Yokokawa, H. Harada, M. Enomoto, Modeling the microstructural evolution of Ni-base superalloys by phase field method combined with CALPHAD and CVM, *Comp Mater Sci.* 39 (2007) 871–879.
- [31] T. Wang, G. Sheng, Z.K. Liu, L.Q. Chen, Coarsening kinetics of  $\gamma'$  precipitates in the Ni-Al-Mo system, *Acta Mater.* 56 (2008) 5544–5551.
- [32] U. Grafe, B. Bottger, J. Tiaden, S.G. Fries, Coupling of multi-component thermodynamic databases to a phase field model: application to solidification and solid state transformations of superalloys, *Scripta Mater.* 42 (2000) 1179–1186.

- [31] L.Q. Chen, Phase-field models for microstructure evolution, *Annu. Rev. Mater. Res.* 32 (2002) 113–140.
- [32] Y. Wang, L.Q. Chen, A.G. Khachaturyan, Kinetics of strain-induced morphological transformation in cubic alloys with a miscibility gap, *Acta Mater.* 41 (1993) 279–296.
- [33] Y. Wang, L.Q. Chen, A.G. Khachaturyan, Shape evolution of a precipitate during strain-induced coarsening - a computer simulation, *Scripta Mater.* 25 (1991) 1387–1392.
- [34] Y. Wang, L.Q. Chen, A.G. Khachaturyan, Strain-induced modulated structures in two-phase cubic alloys, *Scripta Mater.* 25 (1991) 1969–1974.
- [35] Y. Wang, D. Banerjee, C.C. Su, A.G. Khachaturyan, Field kinetic model and computer simulation of precipitation of  $L1_2$  ordered intermetallic from FCC solid solution, *Acta Mater.* 46 (1998) 2983–3001.
- [36] D. Banerjee, R. Banerjee, Y. Wang, Formation of split patterns of  $\gamma'$  precipitates in Ni-Al via particle aggregation, *Scripta Mater.* 41 (1999) 1023–1030.
- [37] M. Cottura, Y. Le Bouar, B. Appolaire, A. Finel, Role of elastic inhomogeneity in the development of cuboidal microstructures in Ni-based superalloys, *Acta Mater.* 94 (2015) 15–25.
- [38] A. Gaubert, M. Jouiad, J. Cormier, Y. Le Bouar, J. Ghiggi, Three-dimensional imaging and phase-field simulations of the microstructure evolution during creep tests of <011>-oriented Ni-based superalloys, *Acta Mater.* 84 (2015) 237–255.
- [39] A. Gaubert, Y. Le Bouar, A. Finel, Coupling phase field and viscoplasticity to study rafting in Ni-based superalloys, *Philos. Mag.* 90 (2010) 375–404.
- [40] J. Kundin, L. Mushongera, T. Goehler, H. Emmerich, Phase-field modeling of the  $\gamma'$ -coarsening behavior in Ni-based superalloys, *Acta Mater.* 60 (2012) 3758–3772.
- [41] M. McCormack, A.G. Khachaturyan, J.W. Morris, A two-dimensional analysis of the evolution of coherent precipitates in elastic media, *Acta Metall. Mater.* 40 (1992) 325–336.
- [42] M.S. Bhaskar, Quantitative phase field modelling of precipitate coarsening in Ni-Al-Mo alloys, *Comp. Mater. Sci.* 146 (2018) 102–111.
- [43] F. Michael, S. Felix, H. Markus, G. Uwe, Phase-field modeling of precipitation growth and ripening during industrial heat treatments in Ni-base superalloys, *Metall. Mater. Trans. A* 49 (2018) 4146–4157.
- [44] I. Steinbach, F. Pezzolla, B. Nestler, M. Seeßelberg, R. Prieler, G.J. Schmitz, L.L. Rezende, A phase field concept for multiphase systems, *Phys. D* 94 (1996) 135–147.
- [45] J.W. Cahn, J.E. Hilliard, Free energy of a nonuniform system. I. Interfacial free energy, *J. Chem. Phys.* 28 (1958) 258.
- [46] J.W. Cahn, On spinodal decomposition, *Acta Metall.* 9 (1961) 795–801.
- [47] S. Komura, H. Furukawa, Dynamics of Ordering Processes in Condensed Matter, Springer, US, 1988.
- [48] C.Y. Teng, N. Zhou, Y. Wang, D.S. Xu, A. Du, Y.H. Wen, R. Yang, Phase-field simulation of twin boundary fractions in fully lamellar TiAl alloys, *Acta Mater.* 60 (2012) 6372–6381.
- [49] M.P. Gururajan, T.A. Abinandanan, Phase field study of precipitate rafting under a uniaxial stress, *Acta Mater.* 55 (2007) 5015–5026.
- [50] H. Ramanarayanan, T.A. Abinandanan, Phase field study of grain boundary effects on spinodal decomposition, *Acta Mater.* 51 (2003) 4761–4772.
- [51] T.A. Abinandanan, F. Haider, An extended Cahn-Hilliard model for interfaces with cubic anisotropy, *Philos. Mag. A* 81 (2001) 2457–2479.
- [52] S. Biner, Bulent, Programming phase-Field Modeling, Springer, Berlin, Germany, 2017.
- [53] X.Y. Sun, C.L. Chen, L. Yang, L.X. Lv, S. Atroshenko, W.Z. Shao, X.D. Sun, L. Zhen, Experimental study on modulated structure in alnico alloys under high magnetic field and comparison with phase-field simulation, *J. Magn. Magn. Mater.* 348 (2013) 27–32.
- [54] A.G. Khachaturyan, S. Semenovskaya, T. Tsakalakos, Elastic strain energy of inhomogeneous solids, *Phys. Rev. B* 52 (1995) 15909.
- [55] A.G. Khachaturian, Theory of Structural Transformations in Solids, dover publications, New York, USA, 1983.
- [56] S.J. Wang, R.F. Sekerka, A.A. Wheeler, B.T. Murray, S.R. Coriell, R.J. Braun, G.B. McFadden, Thermodynamically-consistent phase-field models for solidification, *Phys. D* 69 (1993) 189–200.
- [57] T. Hong, A.J. Freeman, Effect of antiphase boundaries on the electronic structure and bonding character of intermetallic systems: niAl, *Phys. Rev. B Condensed Matter* 43 (1991) 6446–6458.
- [58] H. Nitta, T. Yamamoto, R. Kanno, K. Takasawa, T. Iida, Y. Yamazaki, S. Ogu, Y. Lijima, Diffusion of molybdenum in  $\alpha$ -iron, *Acta Mater.* 50 (2002) 4117–4125.
- [59] COMSOL Ltd. COMSOL Multiphysics, 2019 URL: <<https://www.comsol.com/>>.
- [60] S. Dewitt, S. Rudraraju, D. Montiel, W.B. Andrews, K. Thornton, Prisms-PF: a general framework for phase-field modeling with a matrix-free finite element method, *npj Comput. Mater.* 29 (2020) 1–12.
- [61] COMSOL Multiphysics 5.4 user's guide, COMSOL U.S.A. 2018.
- [62] I. Schmidt, D. Gross, Directional coarsening in Ni-base superalloys: analytical results for an elasticity-based model, *Proc. R. Soc.: math. Phys. Eng. Sci.* 455 (1999) 3085–3106.
- [63] A.V. Ponomareva, Y.K. Vekilov, I.A. Abrikosov, Effect of Re content on elastic properties of B2 NiAl from ab initio calculations, *J. Alloys Compd.* 586 (2014) 274–278.
- [64] A.G. Every, A.K. McCurdy, Second and higher order elastic constants, *Landolt-Börnstein Condensed Matter* 29 (1992) 638–641.
- [65] J. Roesler, H. Harder, M. Baeker, Mechanical Behaviour of Engineering Materials Metals, Springer, Heidelberg, 2007.
- [66] Project Jupyter, Jupyter notebook, 2019. URL: <<https://jupyter.org/>>.
- [67] G. Simmons, H. Wang, Single Crystal Elastic Constants and Calculated Aggregate properties: A Handbook, MIT Press, Cambridge, MA, USA, 1971.
- [68] P. Söderlind, R. Ahuja, O. Eriksson, J.M. Wills, B. Johansson, Crystal structure and elastic-constant anomalies in the magnetic 3d transition metals, *Phys. Rev. B Condensed Matter* 50 (1994) 5918–5927.
- [69] Y.Y. Zhao, H.W. Chen, Z.P. Lu, T.G. Nieh, Thermal stability and coarsening of coherent particles in a precipitation-hardened  $(\text{NiCoFeCr})_{94}\text{Ti}_2\text{Al}_4$  high-entropy alloy, *Acta Mater.* 147 (2018) 184–194.
- [70] T. Philippe, P.W. Voorhees, Ostwald ripening in multicomponent alloys, *Acta Mater.* 61 (2013) 4237–4244.
- [71] C.J. Kuehmann, P.W. Voorhees, Ostwald ripening in ternary alloys, *Metall. Mater. Trans. A* 27 (1996) 937–943.